communications earth & environment

Article

https://doi.org/10.1038/s43247-024-01665-4

Tracking the 2007–2023 magma-driven unrest at Campi Flegrei caldera (Italy)

Ana Astort[1], Elisa Trasatti[1] ✉, Luca Caricchi[2], Marco Polcari[1], Prospero De Martino[3], Valerio Acocella[4] & Mauro A. Di Vito[3]

Understanding and managing unrest at a volcano include i) ascertaining the magmatic distribution and migration, and ii) tracking the evolution of the shallow plumbing system. Here we use multi-technique geodetic data, mechanical models, and petrological simulations to define both aspects for the ongoing (2005-present) unrest at Campi Flegrei caldera, Italy. Results show a deformation source exhibiting progressive widening and shallowing, from 5.9 to 3.9 kilometres. Concurrently, a deeper tabular source at 8 km depth experiences limited but constant deflation. Petrological calculations explain inflation of the shallower source resulting from the rise of 0.06 to 0.22 cubic kilometres of magma from depth ≥8 kilometres. Our analysis provides strong evidence that magma ascent to depths shallower than 8 kilometres is the ultimate driver behind the ongoing unrest. This merging of geodetic and petrological approaches to track the evolution of a plumbing system better constrains magma ascent at volcanoes experiencing unrest.

In order to properly assess the probability to have an eruption during unrest at a volcano, it is imperative to ascertain the distribution of magma in the shallow plumbing system, as well as to track its migration[1]. Critical observables include the depth and size of the melt pockets, as well as their relative magma transfer, with the ultimate aim to promptly recognize any rise of shallow magma towards the surface[2]. Such monitoring becomes particularly important for long-lasting unrest episodes at volcanoes in densely inhabited areas. Here the unrest should be monitored to timely track the evolution of the shallow plumbing system responsible for unrest. A commonly monitored feature is the deformation of the volcano at the surface. This may be ascribed to variations in the pressure of the source(s) below[3]. In this frame, geodetic data are collected and inverted to define the location and size of the deformation source(s). A common limitation of this approach resides in the unknown nature of the pressure source, usually assuming that deeper sources are magmatic, and shallower are hydrothermal. In some cases, a source may exhibit intermediate depths (3-4 km) that may be poorly diagnosed. This is the case of the Campi Flegrei (CF) caldera, Italy (Fig. 1), whose main source responsible for the recent and ongoing unrest episodes has been inferred to lie at intermediate depths, raising contrasting hypotheses on its magmatic or hydrothermal nature[4–13]. Here, we attempt to better constrain the nature of the shallow source at CF by merging geodetic and numerical modelling studies with petrological calculations.

After the last 1538 CE eruption, recent activity at CF culminated in three unrest episodes in the 20th century between 1950–1952, 1969–1972, and 1982–1984, involving uplift in the central part of the caldera (Pozzuoli area) of ~0.7, ~1.7, and ~1.8 m, respectively[10,14]. The caldera has been then slowly uplifting at increasing rates since 2005, as documented by the GNSS network[14–16] and InSAR (Interferometric Synthetic Aperture Radar) analysis[17]. From 2005 to December 2023, the cumulative uplift reached 119 ± 0.3 cm at Pozzuoli[18] (Fig. 1c). During the 1982–84 unrest, CF experienced more than 16.000 earthquakes[19]. From 1984 to 2005, rare seismic events took place. The caldera reawakening in 2005 was accompanied by low rates of seismicity (Fig. 1a, c). This then became progressively more intense[16,20–22]. In particular, in 2012 a seismic swarm took place, and since 2014 the seismicity rate increased nearly exponentially (Fig. 1c), ultimately challenging the Italian Civil Protection[23] on a seismic crisis involving also a few Md > 3.5 events at depth <3 km since February 2023, peaking in August-October 2023.

CF is also characterized by a hydrothermal system, undergoing a considerable increase in degassing rates up to ktons/day and changes in the geochemistry in the Solfatara-Pisciarelli fumarolic field, 2 km NE from Pozzuoli[24–26]. The spatial and temporal changes in the seismicity patterns have been interpreted as due to magmatic fluid circulation and permeability increase within the hydrothermal system[10,22,27], overall regulated by the high temperature of the crustal rocks and CO_2 emissions[10,28–30]. Petrological and geochemical analyses[10,11,26] attribute a large amount of the gas emitted during the unrest to originate from the deep magmatic system located at depths ≥ 8 km, in accordance with the evidence of a layer with 80–90% melt at

[1]Istituto Nazionale di Geofisica e Vulcanologia, National Earthquake Observatory, Rome, Italy. [2]Department of Earth Sciences, University of Geneva, Geneva, Switzerland. [3]Istituto Nazionale di Geofisica e Vulcanologia, Osservatorio Vesuviano, Naples, Italy. [4]Department of Science, Università degli Studi di Roma Tre, Rome, Italy. ✉e-mail: elisa.trasatti@ingv.it

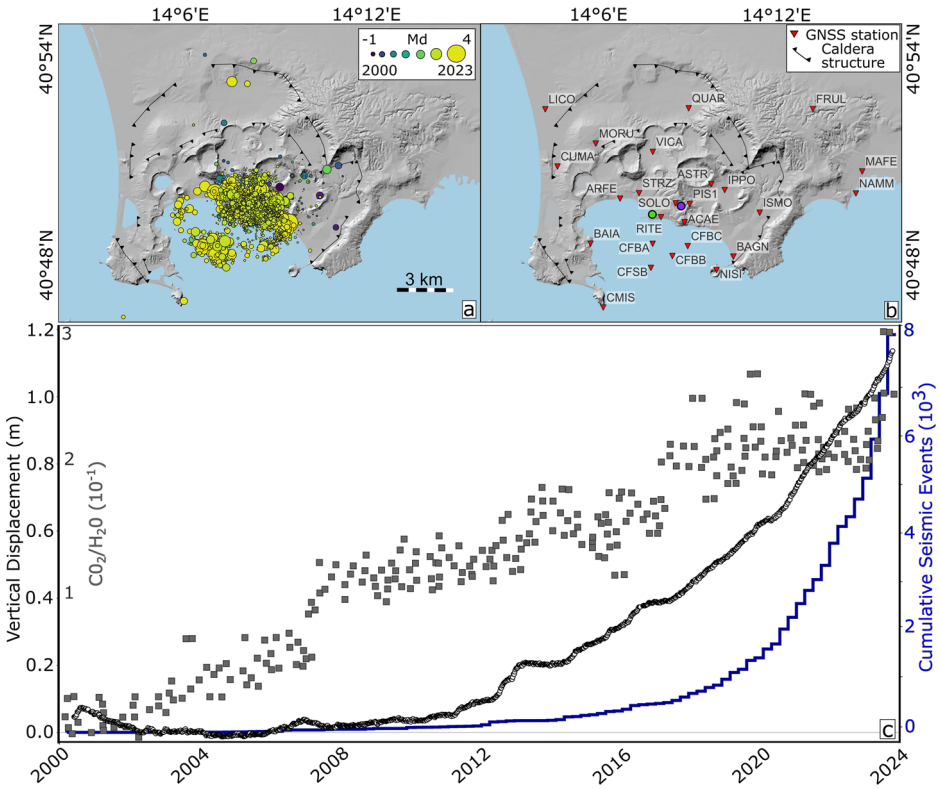

Fig. 1 | Monitoring data of Campi Flegrei caldera (Italy). a Seismicity during 2000-2023 (the circle size represents the seismic duration magnitude Md, while the colour indicates the date of the seismic event), with the principal structures of the Campi Flegrei caldera. Seismic data from https://terremoti.ov.ingv.it/gossip/. **b** GNSS network (red triangles) and the location of Pozzuoli town (green) and Solfatara area (purple). **c** Vertical displacement time series measured at the GNSS RITE station sited in Pozzuoli (black dots), cumulative number of seismic events (blue line) and the CO_2/H_2O ratio (grey squares). Data from Osservatorio Vesuviano INGV[18].

about 7.5 km[31]. The repeated unrest episodes have been suggested to have modified the thermal and rheological behaviour of the crust at CF, evolving towards conditions more favourable for eruption[10,32,33].

Different periods of the ongoing unrest have been investigated exploiting geodetic data and modelling[5,6,34–38]. Although there are differences in the adopted modelling techniques, obtained source depths and retrieved volumes, all models agree that the main source of surface deformation is located at depth > 3 km. Above this depth, there is a low Vp and high Vp/Vs zone, identified as a fractured volume affected by hydrothermal circulation[29–31,39]. Most of the models also agree that the source has sill-like shape (penny-shaped crack or oblate spheroid). However, the assumption of a homogeneous or heterogeneous medium at CF caldera generates variable modelled depths for the source (~2.5 to 3 km in the homogeneous case and 3.6 to ~5 km in the heterogeneous case). The activity of a deeper (≥ 8 km depth) reservoir on the deformation has been seldom investigated, although it has been argued that magma accumulation at a depth > 7 km contributes to the observed caldera deformation since 2015 at least[38]. Other studies show that the transfer of magma from the deeper reservoir to a shallower source was not fully constrained for the 2011–2013 period[6], even though strongly suspected for the 1982–84 unrest[40]. Historical and archaeological records have also highlighted the pressurization of this deeper reservoir before and after the last 1538 eruption[41,42].

As anticipated, the mechanisms driving the ongoing unrest at CF are still debated. From multidisciplinary geophysical and geochemical studies, there is a general agreement in considering the deeper source at 8 km depth of magmatic origin[11,31,43,44]. However, the magmatic or hydrothermal nature of the shallower deformation source at approximately 4 km, and its relationship with the deep plumbing system, has remained unclear so far[4–12,30,37]. Ongoing uplift has been attributed either to magma intrusion, fluid migration or perturbation in the pressure and temperature conditions of the hydrothermal system, possibly caused by degassing from a crustal magma chamber. A recent 4D tomography corroborates the hypothesis of a two-source plumbing system below the centre of the caldera, identifying a 4.5–5 km deep magmatic body since 2019[45]. Understanding the nature of the current unrest is paramount for evaluating its potential for any eruption.

This work aims at better constraining the ongoing unrest at CF, in terms of location, size evolution and nature of the involved sources. To this aim, we consider different sets of geodetic data, including inland and offshore GNSS networks and SAR images on the ongoing unrest, defining seven intervals in the non-linear trend of uplift from 2007 to 2023. Taking advantage of the FEM (Finite Element Method), we account for the elastic structure of the local crust, as inferred by merging active and passive seismic tomographies. The model of the plumbing system consists of a shallower and a deeper source. The shallower source shape is not fixed a priori, but obtained by its implicit representation as a moment tensor, while the deeper reservoir is fixed at 8 km. Once we retrieve their variations in volume and location (the latter only for the shallower source), we perform petrological simulations of mass balance to constrain their nature and mass transfer. These models suggest that realistic scenarios should account for magma ascent from the deeper reservoir, associated with degassing and outgassing.

Results and discussion

Geodetic data time-series

Our analysis begins in 2007, when noticeable deformation rates started. The GNSS data and the multi-temporal InSAR analysis results of the ENVISAT (2007–2011) and COSMO-SkyMed (2011–2023) satellite missions show an increasing rate of uplift at the caldera centre (Fig. 2). The consistence between the GNSS and InSAR data cross-validates the inflation pattern[17]. The affected area presents a nearly radial deformation pattern with the maximum displacement focused near the GNSS RITE station, in the caldera centre. The available GNSS seafloor displacements during 2017–2020[46] show that the radial pattern extends also to the submerged part of the caldera (Fig. 2c, d). The vertical displacement from 2007 to 2023 culminates with 117 cm at RITE, to decrease radially outwards and approach negligible values along the caldera boundary (Fig. 2). Based on the first-order displacement variations in the time series of RITE (Fig. 2e), seven time intervals are identified: 2007–2011 (T1), 2011–2013 (T2), 2013–2015 (T3), 2015–2017 (T4), 2017–2020 (T5), 2020–2022 (T6), and 2022-2023 (T7). A general increase of the mean displacement rate is evidenced throughout these intervals, even if second-order fluctuations are present. Particularly, at

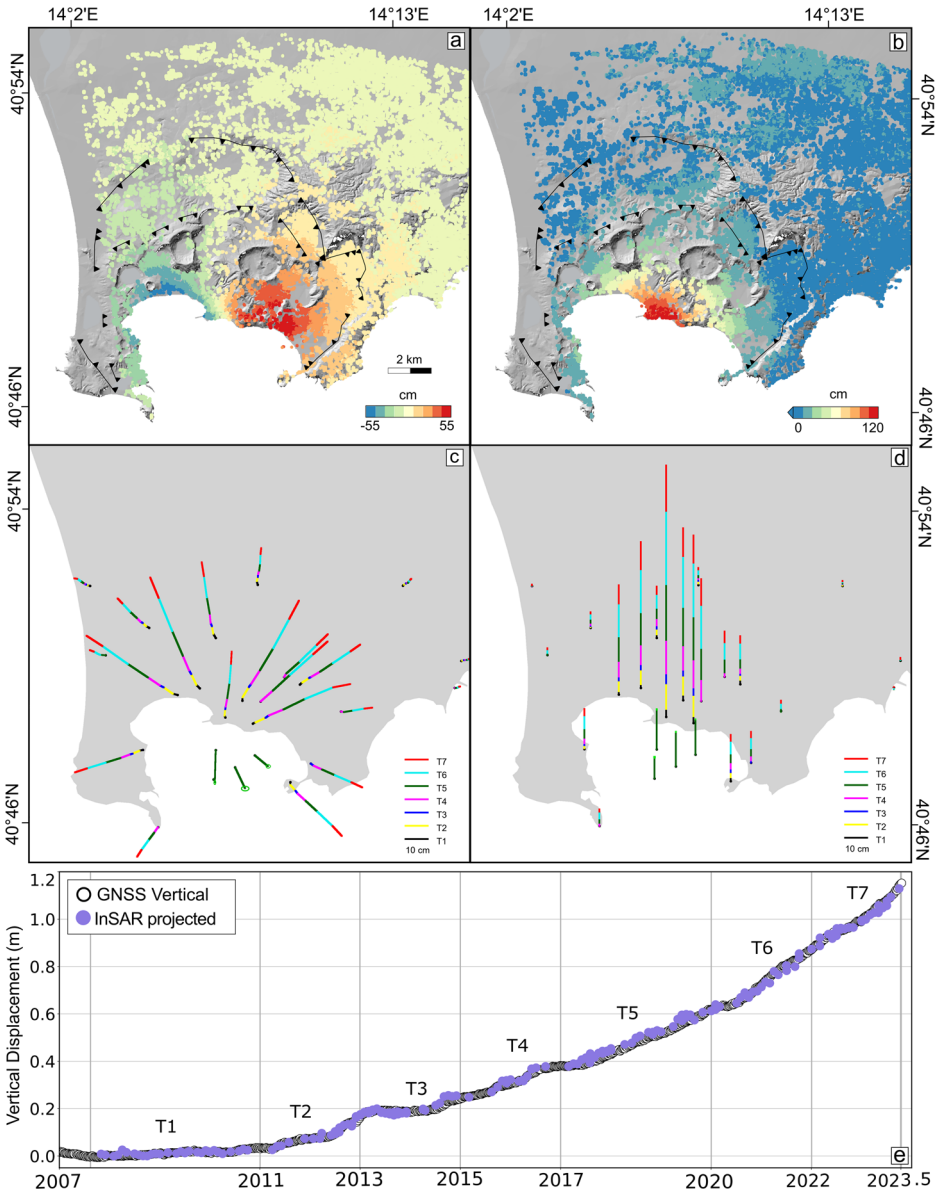

Fig. 2 | Geodetic data during 2007-2023. a, **b** East-West and vertical cumulated displacements, respectively, obtained combining InSAR ENVISAT ascending and descending data (2007–2011) and COSMO-SkyMed ascending and descending data (2011–2023). **c**, **d** Horizontal and vertical GNSS cumulated displacements, respectively, separating seven time periods during 2007–2023. **e** Vertical displacement time series measured at RITE (black dots) and projected vertical time series from ENVISAT and COSMO-SkyMed datasets (lilac dots). The vertical bars identify the seven time periods used in the study.

the RITE station the mean vertical ground velocities for each interval are: 1.1 ± 0.4 cm/yr in T1; 5.8 ± 0.7 cm/yr in T2; 2.3 ± 0.7 cm/yr in T3 (this lower value is attributable to the plateau at the beginning of 2013); 7.6 ± 0.7 cm/yr in T4, 9.1 ± 0.1 cm/yr in T5; 15.2 ± 0.7 cm/yr in T6; and 15.9 ± 0.7 cm/yr in T7. Accordingly, the InSAR ENVISAT and COSMO-SkyMed analysis results with the GNSS data have been spliced based on the seven intervals (details in the Supplementary Table 1). T5 includes the seafloor deformation measurements from 2017 to 2020[15].

FEM modelling of the deformation

The source modelling of the mean ground velocities of the seven periods identified from the GNSS and InSAR data is based on the FEM. The numerical model is purely elastic and accounts for the local heterogeneous elastic structure down to 5 km depth (Methods, and Fig. 3). The 3D elastic structure of CF is calculated from two tomographies with different spatial resolutions[30,39]. The plumbing system consists of a shallower source, whose shape is not fixed a-priori, and a caldera-wide deeper reservoir lying at 8 km depth (Methods, and Fig. 3). The two-step inverse method performs a Bayesian inference[6,40,47–50] on the geodetic velocities during each spliced time window. It retrieves the optimal element-source representing the shallower source, the intensity of the three orthogonal dipoles applied to it (possibly describing a triaxial ellipsoidal cavity[6,40,49–51]) and also the overpressure within the deeper source. The 1D and 2D marginal distributions of the parameters in the seven analysed periods are shown in the Supplementary Figs. 1–9. Although the generalisation of the shallower deformation source in terms of stress tensor is likely subject to multiple global minima, considering only the three diagonal components approach, avoiding the off-diagonal components, helps retrieve unimodal distributions in most cases.

The mean parameters obtained with the inversions are reported in the Supplementary Table 2, while the source parameters (e.g., axes ratios and volume variations), calculated after further analysis of the inversion results (Methods), are reported in Table 1. A linear rate is assumed for each time period and for all modelled quantities (e.g., stress and volume variation). A summary of the two-source plumbing system associated during the time periods considered, based on the results in Table 1, is reported in Fig. 4, including the related seismicity. The latter concentrates above the shallower source and to the NE of the sources centre projections. The shallower source shows two main characteristics: i) it shallows from 2007 to 2015, reaching a stable depth from 2015 to 2023; ii) it grows alternating horizontal widening and overall volumetric increase from 2007 to 2015, followed by only

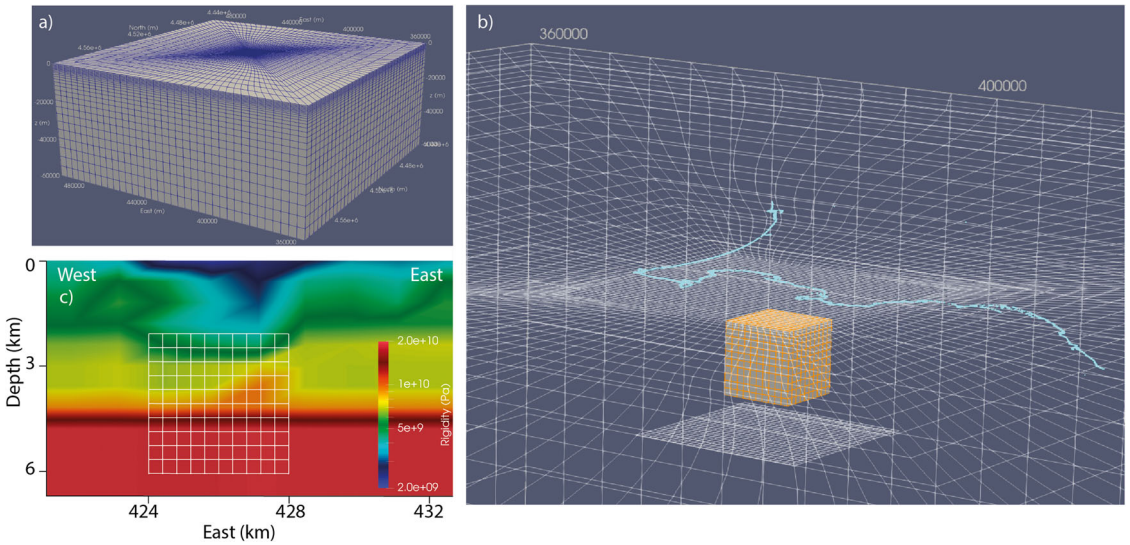

Fig. 3 | 3D FEM modelling of the CF caldera. a Full extension of the FEM computational domain. **b** Detail in the centre of the finite element grid, showing the 1000 potential shallow element-sources (orange volume) and the deep reservoir (white square). The coastline of CF is superimposed in light blue. **c** View from south of a E-W profile passing through the centre of the caldera, showing the rigidity distribution within the FEM domain. The vertical section shows the volume of the potential element-sources with white lines.

Table 1 | Characteristics of the retrieved sources

[a] Time window	[b] Depth (km)	[b] b/a	[b] c/a	[b] ΔV/Δt (10^6 m^3/yr)	[b] ΔV (10^6 m^3)	[b] V_0 (10^6 m^3)	[c] $\Delta V^{deep}/\Delta t$ (10^6 m^3/yr)	[c] ΔV^{deep} (10^6 m)
T1	5.9 ± 0.6	0.62	0.56	1.4 ± 0.2	4.4 ± 0.7	100 ± 0	−0.05 ± 0.03	−0.16 ± 0.12
T2	5.5 ± 0.2	0.99	0.001	5.0 ± 0.4	11.6 ± 0.9	104 ± 1	−0.46 ± 0.03	−1.10 ± 0.06
T3	5.1 ± 0.6	0.77	0.68	2.9 ± 0.3	5.6 ± 0.6	116 ± 2	−0.20 ± 0.03	−0.40 ± 0.06
T4	3.9 ± 0.2	0.34	0.20	4.5 ± 0.5	9.0 ± 1.0	122 ± 2	−0.16 ± 0.03	−0.34 ± 0.06
T5	3.9 ± 0.2	0.97	0.61	2.8 ± 0.4	8.2 ± 1.2	131 ± 3	−0.08 ± 0.03	−0.25 ± 0.09
T6	3.9 ± 0.2	0.76	0.68	5.9 ± 0.5	12.3 ± 1.1	139 ± 5	−0.57 ± 0.03	−1.20 ± 0.06
T7	3.9 ± 0.2	0.74	0.69	8.7 ± 0.7	10.4 ± 0.8	151 ± 6	−1.06 ± 0.03	−1.32 ± 0.03
Final					61.6 ± 6	162 ± 6		−4.81 ± 0.48

[a]T1: 2007–2011; T2: 2011–2013; T3: 2013–2015; T4: 2015–2017; T5: 2017–2020, T6: 2020–2022, T7: 2022–2023.
[b]Shallower source (source depth, ellipsoid's axes ratios with semi-axes $c < b < a$, volume V_0, volume variation ΔV).
[c]Volume variation of the deep source.

volumetric expansion as a thick ellipsoid from 2015 to 2023 (Table 1 and Fig. 4). Between 2007-2011, the deformation source is located at 5.9 ± 0.6 km depth. It becomes shallower during the following years, at 5.5 ± 0.2 km during T2, 5.1 ± 0.6 km during T3, and finally 3.9 ± 0.2 km during T4-T7. T1 and T3 present higher uncertainty on the source depth, and therefore are the less constrained inversions. This is due to the limited deformation taking place at the beginning of the unrest (≤ 1.1 cm/yr in T1) and the low signals characterizing T3 (≤ 2.3 cm/yr), in both cases leading to a low signal-to-noise ratio and therefore to a wider ensemble of similarly fitting models. The interpretation of the source shape, based on the ratios among the retrieved dipoles, highlights a triaxial ellipsoid, except for T2 (Supplementary Fig. 9). Indeed, T1 and T3-T7 fall into the area of possible ellipsoids of different shapes. From the analysis of the dipole orders and ratios, the minor axis *c* is vertical, while the major axis *a*, is oriented along E-W, and *b* is oriented along N-S (except for T7, in which the N-S and vertical axes are switched). In T1 the ellipsoid has an aspect ratio of about 0.5–0.6 along the N-S and vertical axes, representing an E-W oriented prolate spheroid. The source for T2 is the only non-ellipsoidal one. It is very close to that retrieved for the same period, 2011–2013, using similar data but a 6-component moment tensor from different FEM solutions[6]. The study[6] interpreted the shallower source in terms of a sill-like source subject also to shear stress, likely at the sill tips, due to its expansion. In the present study, the shallow source is interpreted as a collapsed ellipsoid with negligible vertical thickness with respect to the width. It can be noted that the time series in T2 (2011–2013) show a velocity change in 2012 (Fig. 2e), but the models related to 2011-2012 and 2012-2013 separately are similar to those considering the whole period 2011-2013[6]. In T3, the ellipsoid corresponds to a nearly spheroidal source with aspect ratios *b/a* and *c/a* of 0.7–0.8. In T4, the ellipsoid is a thin spheroid with aspect ratio of 0.2-0.3, with E-W oriented major axis. In T5, the source shape is a thick sill, or oblate spheroid, being the axes ratios 1 and 0.6. In the last two periods, T6 and T7, the ellipsoids are nearly spheroidal with aspect ratios similar to T3. The volume variation rates of the shallower source span from 1.4×10^6 m^3/yr in T1 to a maximum of 8.3×10^6 m^3/yr in T7 (Fig. 5 and Table 1). The source volume increases from 0.1 km^3 in 2007 to 0.16 km^3 in 2023, with a net increase of more than 60 million m^3 in 16 years. The overpressures rates are lower than 100 MPa/yr (Supplementary Table 3), except those associated to T3, T6, and T7 >50 MPa/yr. These values should be considered upper bounds since thermal gradients and/or viscoelastic rheology, not accounted in the modelling, would cause their reduction[52,53]. This, in turn, would reduce the volume change estimates.

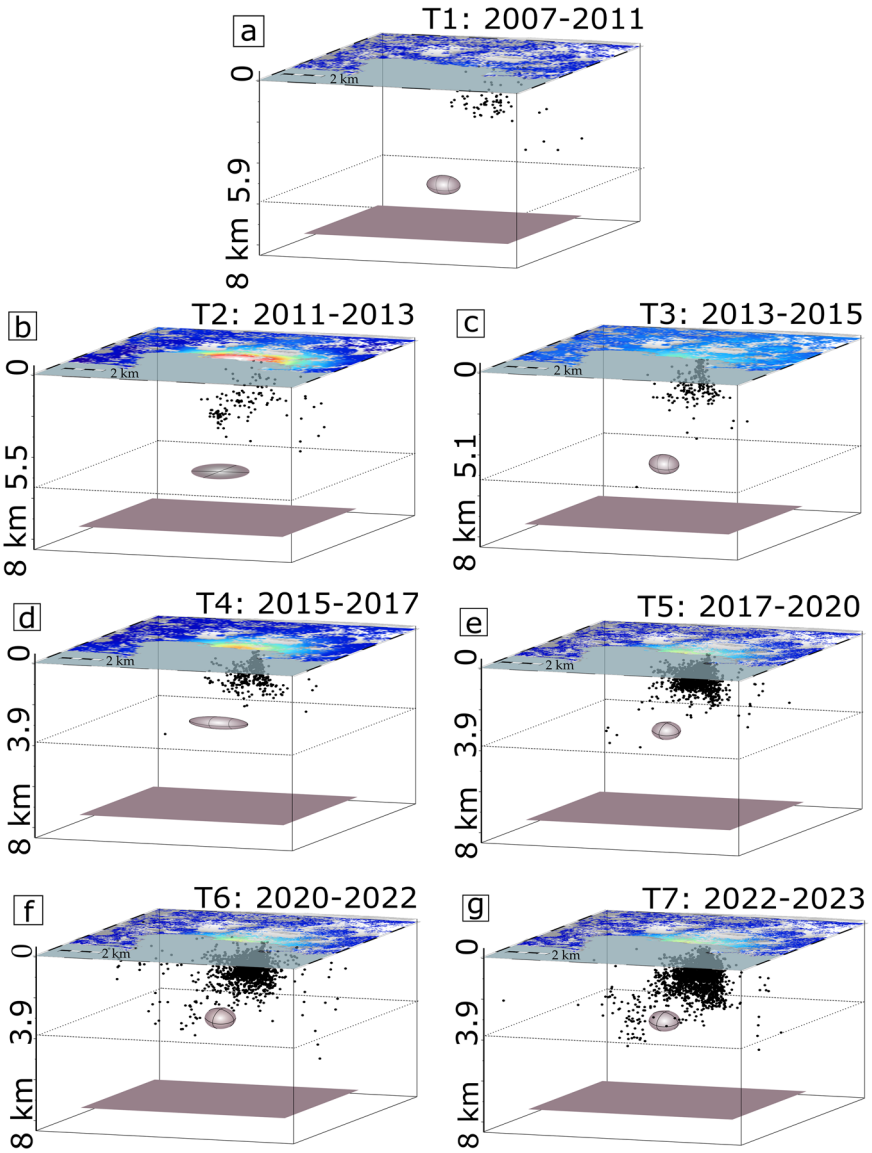

Fig. 4 | Source interpretation from the FEM modelling results from 2007 to 2023. a–g From T1 (a, top left) to T7 (g, bottom right): scaled sketches of the two-source plumbing system of CF from 2007 to 2023. The InSAR descending velocity dataset of each period is superimposed (from -1 cm/yr in blue to 12 cm/yr in red), while the seismicity is shown with black dots. The shallower source dimension is increased by a factor 2.

The deeper source shows limited but persistent deflation through time. Its action is constrained by the inversions from T1 to T7, in which it alternates periods of pressure of -10^3 Pa/yr to -10^4 Pa/yr (Supplementary Table 2) over its area of 100 km^2. By numerical integration of the closure on the tabular source surfaces, the resulting volume variation rate is of the order of -10^4 m^3/yr to -10^6 m^3/yr (Fig. 5 and Table 1). During T7 the total volume variation is the largest, corresponding to -1.3×10^6 m^3 in 1.25 years. The cumulative volume variation of the deep source over the 16 years amounts to approximately -5 million m^3.

Comparisons between observed and modelled InSAR and GNSS data are reported in the Supplementary Figs. 10-11. The residuals show that most of the deformation, both in the near- and far-field, is reproduced and there is no evidence of trends and patterns persisting in the residuals of the three datasets employed in each period, although there are differences in the misfit values (Supplementary Table 2). Even if the number of data points for each period is of the same order (3000–3600 InSAR ascending/descending subsampled data and 14–23 GNSS benchmarks), the signal-to-noise ratio changes, leading to different orders of misfits, despite residuals of the same order in all cases. More interestingly, the signal-to-noise ratio and the misfit obtained by the inversions can be compared. A measure of the signal-to-noise ratio is given by the reduced chi-square of the data vs the uncertainty associated, without the model included in the computation[54]. The reduction of this ratio with the inversions (considering the misfit, i.e., the reduced chi-square, as in the Supplementary Table 2) is as follows: in T1 amounts to 75%, in T2 89%, in T3 90%, in T4 96%, in T5 97%, and in T6 and T7 99.7%. The lowest value in T1 depends on the low initial signal-to-noise ratio of the dataset; a similar consideration applies to T3, and for T2 it results from the aforementioned shear component not fully reproduced by the modelling.

Temporal evolution of the pressure sources

Figure 4 summarizes the sources' shape and position, and the associated seismicity, for each considered period. The beginning of our analysis in 2007 is associated with low seismicity and the shallower source is a horizontal spheroid, at 5.9 km below Pozzuoli. In the next period, T2, the dipoles solutions lay outside the area of possible ellipsoids; because of this uncertainty, the source is here interpreted as sill-like, similarly to previous studies[4–6]. This period was also characterised by renewed seismicity, with a seismic swarm with more than 180 low-magnitude earthquakes in September 2012. At the time, this was the largest swarm since the end of the 1982-84 unrest[21]. Therefore, we interpret T2 resulting from the activity of a volumetric deformation source and an unlocalized shear component that can be associated with the seismicity recorded during 2011–2013. In T3, the source's depth is 5.1 km, with a thicker shape that subsequently shrunk in

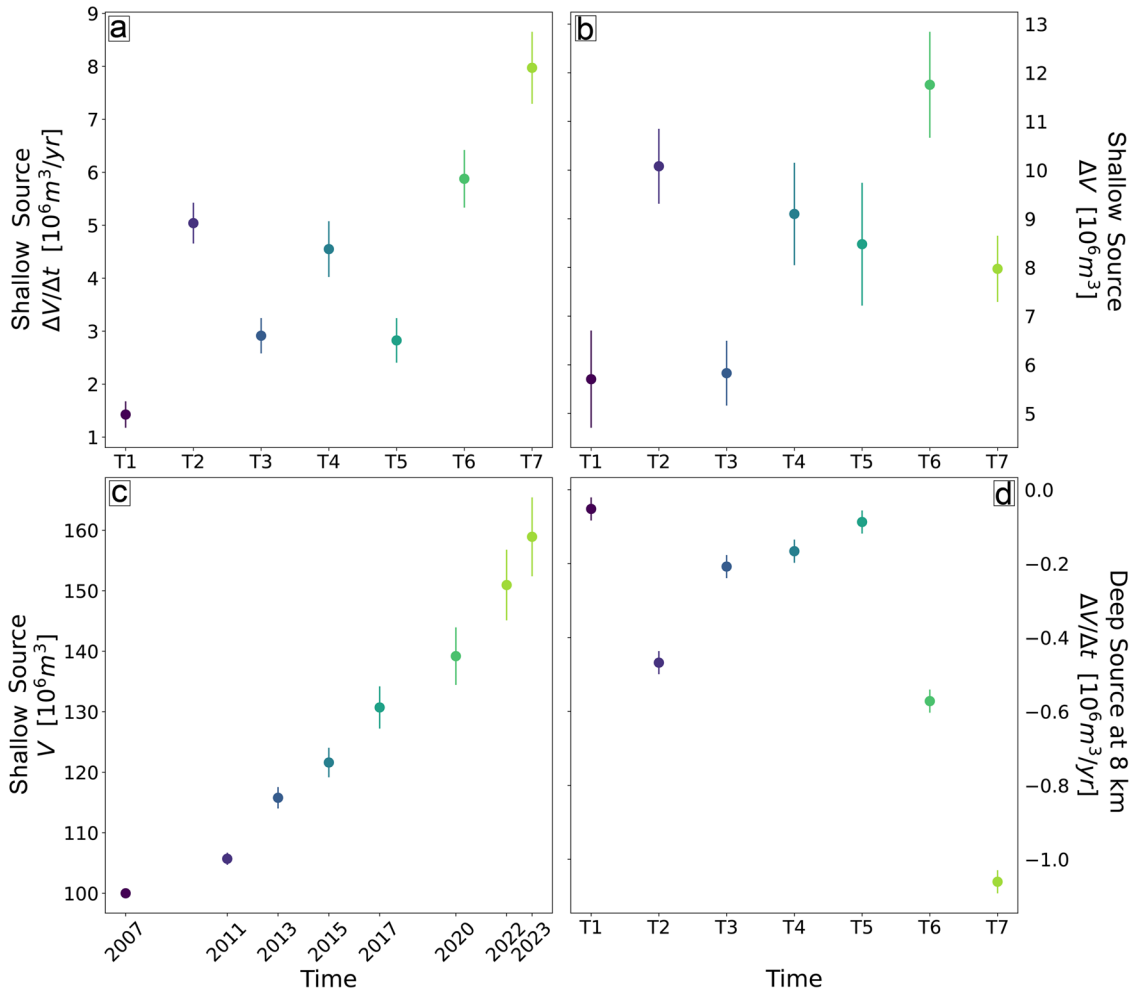

Fig. 5 | Volume variation of the shallower and deeper sources for the periods T1-T7. a Volume variation rate, **b** volume variation, and **c** absolute volume of the shallower source. **d** Volume variation rate of the deeper source.

the north and vertical directions in T4. Since T4 to the end of our analysis (2015–2023), the source depth, 3.9 km, remains constant. The source, a thick oblate horizontal spheroid in T5 and an E-W elongated spheroid during T6 and T7, is surrounded and topped by the hypocentres. We point out that the shallowing of this source is a persistent feature observed also in preliminary inversions employing a spheroid with fixed shape ($b/a = 0.7$ and $a = 800$ m) in a homogeneous medium, and in FEMs without the deep source.

A volume variation rate of about 3×10^6 m^3/yr during 2015–2022 was found previously for the shallower source[38]; it is close to the $4.4 \pm 0.5 \times 10^6$ m^3/yr obtained on average during T4–T6. Our inversions quantified the source volume variations, considering the initial volume of the shallower source in 2007 was equal to 0.1 km^3. This initial volume was estimated as a residual of the unrest episodes of the previous century (see Methods). The initial 0.1 km^3 volume and all the ensuing finite volumes in Table 1 can be considered as minimum estimates. Indeed, there are similarities between the past and recent plumbing systems, e.g., during the pre- and post- eruptive phases of the Monte Nuovo eruption of 1538 CE[41,55], that may have left a larger residual deformation source. Also, the volumes calculated are proportional to the initial volume, so the results would change proportionally to the change in the initial volume.

The deeper source, located at 8 km, is deflating during the whole 2007–2023 period by about 10^4–10^5 m^3/yr, which is one order of magnitude lower than the shallower source volumetric inflation. In terms of time trend, the deeper source shows a behaviour similar to the shallower source. Indeed, when the volume variation rate is the least for the shallower source (T1, T3 and T5), it is also minimum (in absolute) for the deeper one. In T2, T6 and T7 we observe an increase of the volume variation rate in both sources (in absolute for the deeper one). The negative volume variation of the deep source is in accordance with previous findings[40] and the evidence of massive degassing from depths ≥ 8 km[10,11,26]. It should be noted that, given the lower volume variation of the deeper source with respect to the inflating shallower one, the impact of the deeper source on the surface deformation may be not easily detectable (e.g., Supplementary Fig. 12). For this reason, it has been often neglected in previous studies[4–6,35]. Recently, the deep volume variation has been also constrained as positive[38]. This difference in the sign of the deeper source pressurization may be explained by the different data employed (Sentinel-1 instead of COSMO-SkyMed), having different resolving power and processing, different modelling methodology and different number and type of deformation sources. Albeit not questioning previous results, here we propose an alternative two-source plumbing system model for CF, in accordance with geophysical and geochemical indications[10,11,26,31,40]. In the petrologic calculations that follow, we demonstrate that the minor negative variation of the deeper source should be considered as a net in/out value.

The FEM model is heterogeneous down to 5 km depth. Since the deep source is in the homogeneous medium, this may be influencing model predictions in terms of the resulting spatial distribution of stress and deformation. Also, time-dependent inelastic rheologies may affect the deformation pattern. Considering the 16-year time window of our study and assuming typical crustal viscosities (10^{18}–10^{19} Pa s), this period appears compatible with the manifestation of viscoelastic regimes[56]. The viscoelastic

behaviour could play a role and modify our estimates, e.g., changing temporal stress/strain/deformation patterns, and lowering the volume variations and the overpressure estimates. Finally, the high amount of melt of the deeper source[31] does not encourage the use of poro-elastic models, assuming that the high melt percentual has been kept through the years[11,26].

Crustal deformation and seismicity

The epicentres associated with the ongoing unrest show an annular distribution, centred approximately slightly south of Pozzuoli (Fig. 1a), with more intense seismic rates below the Solfatara area. The seismic events are located mostly above 3 km depth, in the hydrothermal system, with only a minor cluster offshore, at ~4 km depth. Our retrieved shallow deformation source rises from 5.9 ± 0.6 km in 2007–2011 to 3.9 ± 0.2 km in 2015–2023, always lying immediately below (or partly to the side) of the hypocentres (Fig. 4).

It has been argued that the continuous activity of the deformation source (mainly the shallower one) during the ongoing unrest is not only measurable at the surface in terms of ground displacement, but it has also induced a permanent stress/strain state in the local crust[32,33]. Here we test this hypothesis by investigating the relation between the stress and strain regime of the CF crust induced by the 16-year-long unrest, as constrained by the retrieved pressure sources, and the distribution of overlying seismicity. We consider the equivalent strain ε^v (i.e., the second invariant of the strain) as a scalar measure of the crustal volumes more susceptible to failure[57] in the seven analysed periods. Our model is purely elastic, and the simulations are ruled only by geodetic constraints. Two representative crustal levels have been considered, at 700 m and 1400 m (Fig. 6), while two others at 1050 m and 2000 m are reported in Supplementary Figs. 13-14. Results show that the strain distribution from our simulations: i) has an annular pattern, with local minimum above the source centre projection (dark orange to red in the center); ii) has the highest strain concentration at a horizontal distance of about 1500-2000 m NE from the source centre projection; iii) decays rapidly at 3 km distance. Moreover, the absolute maximum strain values during each period and at both considered depths are located below the Solfatara area, or between the Solfatara and the coast. Our results show that the 3D elastic structure inferred by the tomographies, and the non-axisymmetric shape of the shallow source of the FEM model play a role in governing the observed patterns of the seismicity, especially since 2015 (from T4 on). These results are in agreement with the actual features of the overall seismicity pattern observed in the ongoing unrest, as illustrated in Figs. 1 and 6. Therefore, the location and evolution of the seismicity show a direct link with the pressurization of the plumbing system during 2007–2023.

Petrological constraints: Evidence of magma and gas ascent at Campi Flegrei

Our modelling results show that from 2007 to 2023 the deep source deflated by a volume of about one order of magnitude lower than the inflation of the shallow source (10^4–10^5 m^3/yr versus 10^6 m^3/yr). In principle, one may expect some relationship between the mass lost in the deeper reservoir and that gained in the shallower one, involving transfer from one reservoir to the other. Here we combine geodetic observations with petrological calculations (details in the Methods) to provide first order estimates of volumetric variations associated with different magmatic processes and thus test the plausibility of different scenarios related to the ongoing unrest (Fig. 7).

Different hypotheses can be formulated regarding the processes controlling any link between shallower inflation and deeper deflation. In this context, it is especially important to determine whether the observed behaviours can be explained exclusively by the migration of fluids, or if magma ascent contributes to the observed inflation of the shallow source. Considering the inflation at shallow depth, we examine different scenarios (Fig. 7): A) the transfer of a volume of only volatiles equivalent to the observed deflation from the deeper to the shallower source; B) the transfer, from one reservoir to the other, of a volume of both volatiles and magma equivalent to the observed deflation; C) exsolution of volatiles at shallow depth associated with cooling and magma crystallization; D) magma ascending, degassing and releasing excess fluids (i.e., outgassing) at some depth above the deeper source; E) established connection between the deeper magma reservoir (>8 km) and the shallower source, involving the transfer of magma up to 4 km depth. These scenarios are discussed below, considering that the volume variation retrieved from the geodetic inversions is a minimum estimate, because of the compressibility of the fluids exsolved from the rising magma[58].

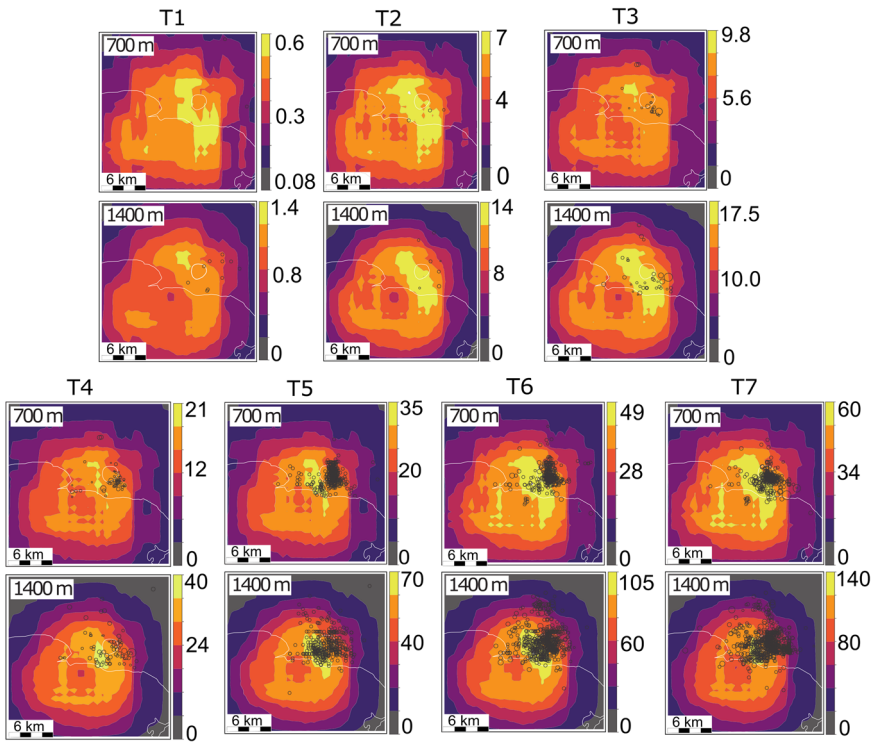

Fig. 6 | Equivalent strain distribution in the crust and associated seismicity for the seven investigated periods. Contours are the equivalent strain ε^v (10^{-5}). The dark grey circles are the seismic events at 700 m and 1400 m, with a buffer of 160 m. In white the coastline and the Solfatara perimeter.

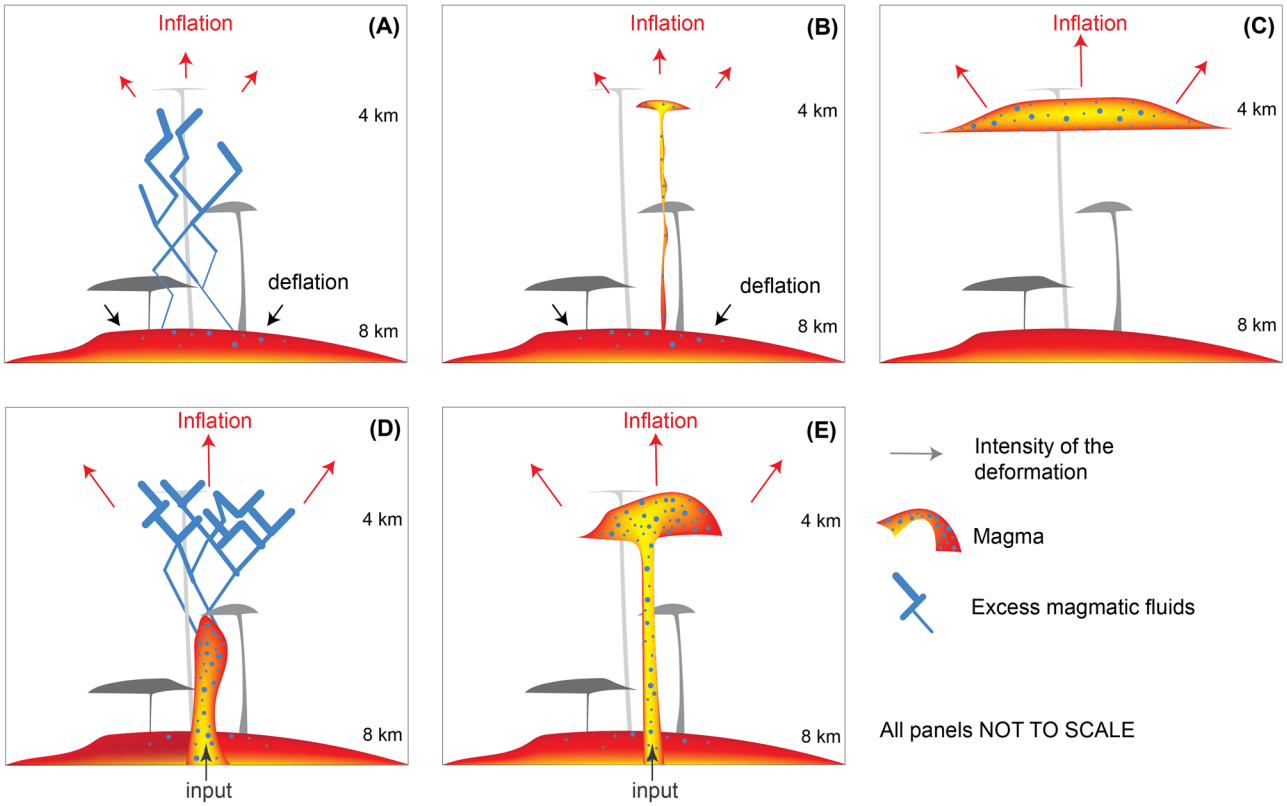

Fig. 7 | Schematic representation of the scenarios considered to potentially account for the geodetic measurements. A–E are the corresponding scenarios described in the main text, and the associated calculations are reported in the Methods. **A** Magmatic fluids are released from the magma at 8 km depth, rising and expanding following the decreasing confining pressure. **B** A volume of magma (containing silicate melt and excess fluids) equivalent to the deflation measured at 8 km depth rises directly to 4 km depth. **C** Previous magma at 4 km depth cools and crystallises, progressively releasing excess fluids. **D** Magma (containing silicate melt and excess fluids) rises from the deep reservoir and releases excess fluids that rise through a fracture network and expand. **E** Similar to **D**, but involving an equivalent volume of magma rising from 8 km to 4 km depth, sufficient to explain the inflation of the shallow source.

Scenario A: the molar volume of fluids at 210 MPa (8 km depth) is 54.99×10^{-6} m^3/mol, while at 100 MPa (4 km depth) is 102.49×10^{-6} m^3/mol. Thus, the transfer of a finite volume of excess gases from 8 to 4 km depth results in a ratio between the volume increase at 4 km (ΔV) and the volume decrease at 8 km (ΔV^{deep}) of 1.86 (102.49/54.99). The ratios estimated from deformation data between deep and shallow sources vary between 28.5 to about 8 (Table 1), which implies that the transfer of a finite volume of only magmatic gases from 8 to 4 km is not sufficient to explain the volumetric variations calculated from the geodetic data.

Scenario B: the coupled transfer of a finite volume of magma and volatiles also cannot explain the geodetic data, because the silicate melt is essentially incompressible with respect to the excess fluids, a feature that would require the decrease of volume of the deep source ΔV^{deep} to be much closer to ΔV. As an example, 0.01 km^3 of magma with 30 vol. % of excess fluids at 8 km will expand to about 0.015 km^3 once reaching 4 km, giving a $\Delta V/\Delta V^{deep}$ of 1.56, still smaller than the volumetric ratio retrieved from geodetic data (Table 1).

Scenario C: we consider that the increase of volume measured geodetically at 4 km depth is caused by crystallization-induced release of magmatic fluids (commonly referred to as "second boiling"[59]; Fig. 7C). The calculations show that 0.12 km^3 of magma would have had to cool to its solidus temperature for a sufficient amount of fluids to be released and cause the inflation. Considering a thermal conductivity of 10^{-6} m^2/s[60] and a spherical reservoir of 0.12 km^3 volume, the timescale of cooling would be of the order of 3000 years, which is larger than the decennial duration of the unrest episode. Because this is a maximum estimate of the cooling timescale, we also computed the timescale of cooling for a sheet of magma of 100 m thickness emplaced at 4 km depth. The timescale is 182 years, which also largely exceed the duration of unrest. Additionally, in this scenario (both cases), the inflation would decrease in time and not increase as observed. Therefore, we deem this scenario not plausible.

Scenario D: we assume that magma rises from 8 km depth and releases excess gases during decompression. In this scenario, the risen magma does not necessarily reach the shallower source. The amount of gases released upon ascent is directly proportional to the volume of ascending magma, the total ascended vertical distance, and the volatile content of magma at 8 km (Methods). For each period we calculate the volume of rising magma required to release enough volatiles to account for the estimated inflation of the shallow source (Fig. 7). The minimum volume of ascending magma is obtained by calculating the volume of excess volatiles released by magma ascending to a depth corresponding to the shallower source. In Fig. 8, our calculations for this scenario show that the minimum volume of ascending magma was 0.019 km^3 in period T3 (felsic magma) and the maximum was 0.052 km^3 in period T2 (mafic magma). The total minimum volume of magma calculated with this approach varies between 0.17 and 0.22 km^3. This is the range of the volume of magma required to reach the shallower source, although it is 3 to 4 times larger than the volume of the inflation of the shallower source retrieved from geodetic data (Table 1). These calculations suggest that either inflation at CF is the result of fluids released by a volume of magma larger than 0.17–0.22 km^3 rising from 8 km depth that did not reach the shallower source, or the inflation is caused by the injection of an equivalent volume of magma and excess fluids in the shallower source. Therefore, it is not possible to univocally determine the stalling depth of the risen magma, as it depends on the volume of the rising magma. Importantly, the deflation at 8 km is much smaller than that associated with the loss of mass required to explain the increase in volume of the shallow source. It is thus necessary that the volume of ascending magma and excess gases is largely compensated by the addition of magma from the portion of the

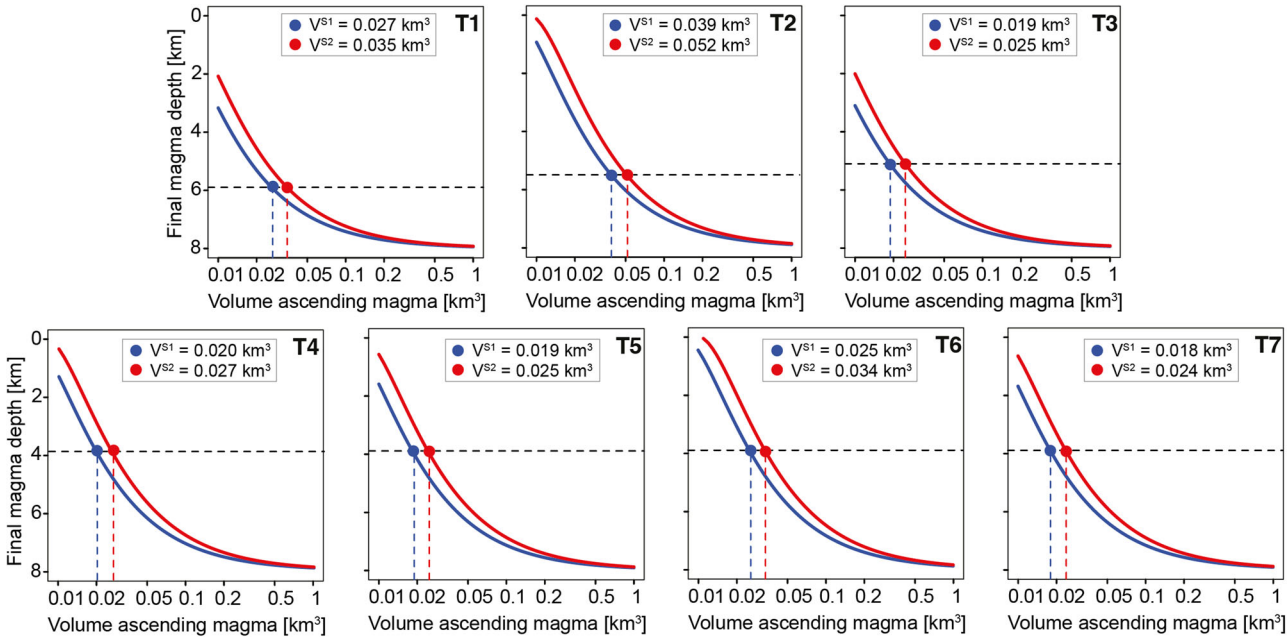

Fig. 8 | Relationship between the volume of ascending magma and the final depth of ascent required to account for the inflation observed (scenario D). The depth of the shallower source estimated from geodetic data is identified by the dashed horizontal line for each period. The final depths of ascent from the simulations are calculated considering the release of pure H_2O from the magma. The blue and red lines are calculated considering a cooler felsic magma and a mafic and hotter one, respectively (Supplementary Fig. 16). The intersecting volumes are identified by the blue and red circles, V^{S1} and V^{S2}, respectively.

magma reservoir located at depths > 8 km. This, in turn, would also imply that the melt portion of the reservoir is maintained.

Scenario E: following the last consideration, a fifth possible scenario is that the inflation of the shallower source is directly connected with the deeper magma reservoir, with the arrival of a volume of magma and volatiles equivalent to the increase in volume of the shallower source (0.06 km³; Table 1). This scenario thus considers plausible the arrival of magma at 4 km depth, provided that the deeper source is recharged from below.

As a last comment, the underplating of basalt at the base of the shallow source may in principle lead to reheating and vesiculation. However, reheating would also result in remelting, and the consequent decrease of fluid concentration in the melt, which will efficiently buffer the release of excess fluids[61]. Also, a large mass of magma would need to be heated up to produce sufficient fluid exsolution to explain inflation. This implies that the mass of basalt that would need to be underplated to heat up the shallow source would need to be even larger than that calculated in scenario C. Finally, the ascent of the underplating magma would release more fluids than those released by reheating. For all these reasons, we discard the potential consequences of magma rising and underplating the shallower source.

Therefore, the two most plausible scenarios (D and E) involve, in addition to the input of magma to 8 km depth, the transfer of magma from the deeper reservoir to shallower levels (up to 4 km depth in case of scenario E), implying the direct involvement of rising magma in the ongoing unrest.

Conclusions

Surface deformation results from 2007 to 2023 at CF suggest the activity of both a shallower and a deeper source (Fig. 9). While the pressurized shallower source exhibits gradual widening and decrease in depth, from 5.9 to 3.9 km, the deeper magmatic source at 8 km depth experiences minor deflation. The mechanical simulations depict strain concentration in agreement with the seismicity location, evidencing not only the direct link between long-term deformation and seismicity, but also the interaction between the shallowest (the hydrothermal system at depth <3 km) and the deeper portions (the plumbing system, at depth ≥ 4 km) of CF during 2007–2023.

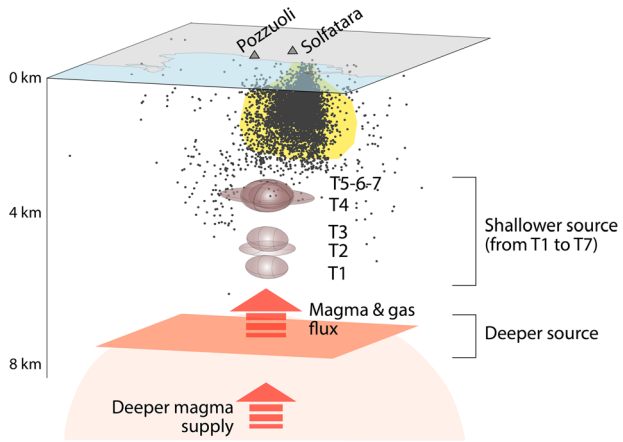

Fig. 9 | Sketch of the 2007-2023 active plumbing system at CF. The shallower sources retrieved by the data inversions during the periods T1-T7 are reported in transparent purple, while the deeper reservoir is in orange. The seismicity is shown with black dots. The yellow volume is the hydrothermal system. The shallower source dimension is increased by a factor 3.

To better define the nature of the shallower source, and any involvement of magma, we employed petrological calculations. These explain the deflation of the deeper source with the rise of 0.06 to 0.22 km³ of magma towards the shallower source, largely compensated by the input of magma from below 8 km depth. The volume of magma ascending towards the shallower source cannot be constrained precisely, as the same volumetric increase can be produced by the release of volatiles from a large volume of magma rising at small depth, or smaller volume ascending more. In any case, all calculations require the ascent of magma from 8 km depth, demonstrating its direct involvement in the unrest.

The FEM model approach developed and tested during the 2007–2023 unrest at Campi Flegrei, merging geodetic and petrological methodologies, can allow tracking the evolution of a plumbing system even in near real time,

better constraining magma ascent in a timely way at volcanoes experiencing unrest.

Methods

GNSS and satellite radar observations

The GNSS dataset consists of 21 inland stations widely distributed in the CF area, plus 2 new seafloor stations located in the Gulf of Pozzuoli[15,46,62] (Figs. 1–2). These stations belong to the NeVoCGPS network and MEDUSA marine infrastructure operated by the Istituto Nazionale di Geofisica e Vulcanologia - Osservatorio Vesuviano (INGV-OV). Even though the dataset has rather heterogeneous dates, especially at the beginning of our analysis, a well-distributed inland GNSS network with 14 stations was available since 2007–2011, and the stations number increased to 21 after 2017[15]. The analysis, based using the Bernese GPS software v. 5.0 on a daily basis has been extended until the end of 2023[62]. Also, two new GNSS seafloor stations were incorporated[46]. We consider only two stations (CFBB and CFBC) out of the four available, since the CFSB buoy, the farthest from the coastline, presents very high noise and CFBA, already accounted only for the vertical component, is characterized by high residuals in all the tests attempted, as previously evidenced[63] and possibly due to the position of CFBA buoy, relatively close to the navigation routes in the gulf.

The employed InSAR time-series data are a subset of the CF open access dataset[17], consisting of a homogeneous and continuous SAR dataset of the CF caldera from 1992 to 2021 and exploiting the acquisitions from three satellite missions in both orbits: ERS 1-2 (1992–2002), ENVISAT (2003–2010) and COSMO-SkyMed (2011–2021). The COSMO-SkyMed ascending and descending datasets have been updated to October 2023. The data were processed by the multi-temporal and multi-baseline approach using the GAMMA software[64], retrieving the CF ground deformation velocity and displacement time series. The obtained InSAR products have been validated using independent GNSS data and levelling measurements, with RMSE below a threshold of 5 mm/yr in each case[17]. Considering the 2007 as the beginning of the evident deformation associated with the unrest and the availability of the GNSS data[15,62], two satellite missions were employed: ENVISAT, covering 2007–2011, and COSMO-SkyMed, covering 2011–2023.

Based on the observations of ground velocity changes in the time series from both GNSS and InSAR data, seven time windows were selected to be modelled separately (Figs. 1–2). The intervals identified are 2007–2011 (T1), 2011–2013 (T2), 2013–2015 (T3), 2015–2017 (T4), 2017–2020 (T5), 2020–2022 (T6), and 2022–2023 (T7). Accordingly, the mean ground velocity for each interval was computed for each dataset, and Supplementary Table 1 reports the exact date intervals for each period. The division in periods has been carried out to minimize the effect of secondary short-time signals on the main pattern (Fig. 2e). Alternative divisions may still be valid. Additionally, the InSAR mean ground velocity for each period has been spatially downsampled with two sample sizes, 300 m in the highly deforming area within a radius of approximately 5 km, and 600 m outside.

FEM - 3D model

The modelling is based on the FEM technique, to account for the elastic structure of CF in the data optimization process and to avoid fixing the shallow source shape a-priori. The model consists of 150,000 8-nodes brick elements (Fig. 3). The computational domain extends 140 km x 140 km x 60 km to ensure negligible displacement and stress at the boundaries. The elements have a side dimension of 400 m in the caldera centre (a subdomain of approximately 15 km x 15 km x 11 km) and increase their size towards the domain periphery. The free surface of the numerical model is flat, given the mild topography of the caldera and the limited impact on the deformation in this case[65].

The 3D model includes the elastic heterogeneous structure based on the integration of two seismic tomographies[30,39], both providing Vp and Vp/Vs. One[39] is based on an active seismic experiment encompassing the entire caldera (25 km x 25 km) with a resolution of 1 km (down to 5 km depth), while the second tomography[30] was obtained from the analysis of the 1984 microseismicity, and it is centred beneath the Pozzuoli - Solfatara area (7 km x 8 km), with a resolution of 100–150 m down to 3.6 km depth. Both tomographies evidence a sharp decrease of Vp/Vs at 1.7–2.5 km, suggesting the absence of magmatic fluids, and the presence of gas saturated rocks. The high Vp and high Vp/Vs volume extending below, down to 4 km, can be associated with partially molten material enriched in fluids[30], while the caldera rim is defined by an almost continuous annular high Vp anomaly[39].

In the numerical model, the Vp and Vp/Vs have been converted into elastic constants (ν, Poisson coefficient, and μ, rigidity) to define the elastic structure element by element in the computational domain, using

$$\nu = ((Vp/Vs)^2 - 2)/2((Vp/Vs)^2 - 2)$$

$$\mu = Vp^2\rho(1 - 2\nu)/(2 - 2\nu)$$

A simplified layered density structure has been considered (density $\rho = 1800$ kg/m^3 from 0 km to 1 km depth, $\rho = 2000$ kg/m^3 from 1 km to 2 km depth, and $\rho = 2500$ kg/m^3 below 2 km depth), based on the AGIP technical report[66]. The elastic structure obtained is characterised by rigidity values 2 GPa < μ < 20 GPa and Poisson coefficient 0.23 < ν <0.31. These parameters are distributed in 3D patterns in the finite element domain. In general, the rigidity values increase with depth, but have also a highly heterogeneous distribution below the Pozzuoli and Solfatara area (Fig. 3). Below 5 km depth, the model is homogeneous with $\mu = 20$ GPa and $\nu = 0.25$.

FEM - forward modelling

The modelling of the plumbing system of the CF consists of a shallower source and a deeper source. The shape of the shallower source is not fixed a-priori[6,40,49,50]. This shallower source, often assumed with a sill-like shape, is here considered as point-source, due to the small ratio between radius and depth[5,34,67]. In our simulations, this deformation source is implicitly described in terms of an equivalent moment tensor[51,68,69], considering that the far field deformation of a pressurised point-source triaxial ellipsoid arbitrarily oriented can be represented by a proper combination of dipoles and double couples. In the FEM implementation, the moment tensor is $M_{ij} = V\sigma_{ij}$ where V is the volume of the finite element considered and σ_{ij} is the stress tensor applied. The 3D surface displacement is $u_k(r) = S_{ij}U_{ij}^k$ where $k = (x, y, z)$, U_{ij} is the 3D surface displacement field due to the application of unitary double forces and double couples (the stress tensor σ_{ij}) to a single element, and S_{ij} are the scale factors of each stress component. The elementary solutions (U_{ij}) are computed in the heterogeneous 3D FEM model described above. The potential element-sources are cubic finite elements of the grid with side $l = 400$ m with $V = l^3$. The forward model of the inversion consists of a matrix volume of 1000 elements (potential element-sources) centred approximately below Pozzuoli[4–6,38] (Fig. 3). The six components of the stress tensor (each one amounting to 1 MPa) are applied over the element faces separately, obtaining a "Green's Functions" matrix consisting of 6000 FEM computed 3D displacement solutions at the 4537 surface nodes of the model. Accuracy tests reproducing the theoretical displacement due to dipoles and double couples, along with the equivalent pressurized cavities, have been performed with FEMs having similar size and extension[40,49].

We consider the contribution to the deformation of a second deeper source, represented by a deep flat layer in the FEM. This source is simplified as a squared crack with side 10 km, laying at 8 km depth, whose centre is fixed at 426.2 km east, 4518.4 km north (UTM projection, zone 33). In this case, an overpressure of 1 MPa is applied to both sides of the crack, obtaining scalable (positive or negative) surface displacement that adds to that due to the element-source. Our approach neglects possible mechanical interactions between the shallower and deeper source.

FEM - inversion

The FEM solutions have been interpolated in the GNSS benchmarks and InSAR data points of each period, considering bi-linear shape functions within the surface element faces. The FEM inversion is designed to find the mean model consisting of the superposition of the two forward sources described in the previous section for each of the seven periods considered. The non-linear inversion framework retrieves the best element-source among the 1000 available, the scale factors of the stress components applied to it, and the scale factor of the overpressure applied to the deep source. The scale values may range from positive to negative.

In order to limit the unknowns and trade-offs, for the shallow source we consider only the dipole solutions U_{ii}, meaning that the equivalent ellipsoidal source's axes are oriented along the *x-y-z* axes, as discussed in the next section. Indeed, the off-diagonal components related to the double-couples are not zero if the ellipsoid has a strike and/or a dip[6,40,49,50]. Although this assumption is a limitation, adding a possible bias to the solutions, it should be considered that the strike and dip angles cannot be well resolved at CF, since almost half of the caldera is submerged and there are only two measurements on the sea (for only 2017–2020). Also, since the "central" shallower source is often retrieved nearby Pozzuoli, we fix its horizontal position at 426.2 km east, 4518.8 km north (UTM projection, zone 33)[6,34,40], which is about 600 m south of RITE in the seaside. Indeed, this position persisted during preliminary tests, considering also the 400 m discretization of the FEM model. With these simplifications, the inverted free parameters are five: the depth and the three scale factors of the diagonal stresses for the shallow source, and the scale factor for the deep source.

The geodetic inversion is carried out in two steps. In the first one, a global optimization algorithm[48] samples the parameters space and searches for the best fit parameters. For each period, 51'000 total models are sampled during 50 iterations. Considering that for each period there are the GNSS and the InSAR ascending/descending orbit datasets, the misfit function associated with the GNSS data is accounted for in the total misfit with a weight of 1/3. The second step is the Bayesian inference on the sampled model space[47], without further comparisons with data, to obtain the mean model for each period. This inversion is based on the MCMC sampling, and about 40 random walks for 3000 iterations have been carried out.

FEM - source interpretation and volume variation

The inversion results for the shallow source are interpreted in terms of the equivalent pressurised source[6,40,51], following the approach briefly summarised here. The scale factors retrieved, S_{ii}, correspond to the stress diagonal values $\sigma_{ij} = S_{ij}$ x 1 MPa related to the single element. Considering that the off-diagonal components are fixed to 0 in the inversion, the principal stresses $\sigma_1 < \sigma_2 < \sigma_3$ are directly retrieved from the inversions and correspond to σ_{xx}, σ_{yy}, and σ_{zz} ordered. From the ratios σ_1/σ_3 and σ_2/σ_3 it is possible to obtain the axes ratios of the ellipsoidal source[51], considering that the ellipsoidal source is a subset of the possible combinations of the principal stress (or principal moment) ratios[6,40,49,50], as shown in Supplementary Fig. 9. We perform a grid search among all the possible combinations of the axes ratios *b/a* and *c/a*, computing the corresponding σ_1/σ_3 and σ_2/σ_3 as in ref. 51 (eq. 12–19) in order to find those closest to our findings. This process defines also the ratio between the overpressure ΔP and σ_3, since it depends on the ellipsoid aspect ratio (*b/a* and *c/a*).

The ratio between the volume variation ΔV and V the volume is[70]:

$$\Delta V/V = \frac{(1-2\nu)\Delta P}{2(1+\nu)\mu}\left(\frac{\sigma_1+\sigma_2+\sigma_3}{\Delta P} - 3\right)$$

Given the point-source approximation, it is possible to determine the volume variation given an estimate of the initial volume of the source. Considering the similarity among the surface displacements during the unrest of 1982–84 and the recent unrest[4,6], the initial volume of the source is estimated by scaling the volume variation of the 1982–84 to the total deformation of the last three unrest episodes since 1950 before the present one. From the levelling and EDM measurements of 1980–1983, the volume variation of the source is estimated as $17–22 \times 10^6$ m^3 for a maximum uplift of 60 cm occurred at the levelling benchmark 25 A (which recorded the maximum vertical displacement at CF and is located 150 m distance from the RITE station)[34,40]. The net uplift at the same benchmark during 1950 (end of the long-term subsidence at CF) and 2007 (beginning of the present analysis) amounts to 3 m[14,71]. Averaging the reference volume variation to 20×10^6 m^3 for the 1980–1983 uplift, we set the initial volume at 0.1 km^3, scaling the deformation by a factor 5 (i.e., the ratio between the cumulated uplift of 3 m and the 60 cm of 1982-84).

The deep source, approximated as a squared crack, is characterized by non-uniform, asymmetrical opening due to the 3D elastic structure, under the effect of a uniform pressure. The volume variation ΔV^{deep} is calculated by numerical integration of the 3D relative displacement of the initially coincident nodes over the element faces laying on the two sides of the crack, as:

$$\Delta V_0{}^{deep} = L^2 \sum_{i=1}^{n} du_i$$

Where du_i is the relative displacement of the *i-th* paired nodes and n is the total number of the paired nodes on the surfaces, 576 in this case. The result is a unitary volume variation of $\Delta V_0{}^{deep} = 20.8 \times 10^6$ m^3, which linearly scales with the ΔP^{deep} found as the fifth parameter by the FEM inversion.

Equivalent strain calculation

We adopt a strain-based formulation to define the damage and fracture model at CF. In the strain-based formulation, the equivalent strain is usually adopted as the (undamaged) energy norm of the strain tensor[57]. The equivalent strain ε^v is defined as the J2-norm of the strain tensor:

$$\varepsilon^v = \sqrt{\frac{1}{2}(\varepsilon_{xx}^2 + \varepsilon_{yy}^2 + \varepsilon_{zz}^2 + 2\varepsilon_{xy}^2 + 2\varepsilon_{yz}^2 + 2\varepsilon_{zx}^2)}$$

We compute seven scenarios by incrementally run forward FEM models, each one loaded with the sources retrieved in the inversions. At the end of each simulation, we obtained the scenario related to the end date of the period. The equivalent strain ε^v has been computed at the end of each FEM simulation at the integration points of each single element of the whole domain. The comparisons with the seismic catalogue are made at two depths of 700 m and 1400 m, and considering a buffer of 160 m.

Petrology calculations

The target of these calculations is to estimate, considering different scenarios, the volume generated by different processes and compare it with the increase of volume of the shallow source (currently located at a depth of 3.9 ± 0.2 km) estimated from geodesy (Supplementary Table 2). These calculations were not performed to perfectly match the observations, but to provide boundaries within which to apply more sophisticated models that will help clarify the causes of the ongoing unrest.

We use the equation of state[72] to calculate the molar volume of magmatic fluids at different depths, and therefore estimate the increase of volume associated with the ascent and decompression of magmatic fluids or magma exsolving fluids (Supplementary Fig. 15). We converted pressure in depth using a density model[39,73]. The pressures estimated below CF are 210 MPa and 100 MPa at 8 and 4 km depth, respectively.

Scenario A: the partial molar volume of H_2O at different pressures and temperatures were performed using the Equation of state[72] and a Python code for the calculations can be find at: https://github.com/forsterite/fugacity/. The molar volume of fluids at 210 MPa and 900 °C is 48.81×10^{-6} m^3/mol, while at 100 MPa is 90.72×10^{-6} m^3/mol. Considering T7 as an example, the moles of magmatic H_2O which could be transferred to 4 km to account for the deflation estimated by geodesy at 8 km depth

(Fig. 7A) is given by:

$$M_{H_2O} = \frac{1.32 \cdot 10^6[m^3]}{48.81 \cdot 10^{-6}[m^3 mol^{-1}]} = 27 \cdot 10^9[mol]$$

If this amount of magmatic H_2O ascends to 4 km depth, it will generate a volumetric expansion of:

$$\Delta V_{4km} = 27 \cdot 10^9\,[mol] \cdot 90.72 \cdot 10^{-6}[m^3 mol^{-1}] = 2.45 \cdot 10^6[m^3]$$

This value is about 5 times smaller than the observed value of 10.4×10^6 m^3 (Table 1) and therefore the transfer and expansion of a finite mass of magmatic fluids from 8 to 4 km cannot account for the inflation estimated from geodesy (Fig. 7A).

Scenario B: this scenario considers that the deflation at 8 km depth represents a finite mass of magma and fluids moving to 4 km depth. Considering the melt as incompressible, the only resulting expansion would be related to the expansion of exsolved fluids and volatile exsolution associated with decompression (Fig. 7B). We first consider the transfer of a magma without excess fluids. In this case, the only increase of volume is related to the exsolution of volatiles. We consider a H_2O-saturated magma containing 5.7 wt.% of H_2O at 210 MPa (about 8 km) that ascend to 100 MPa (about 4 km), where only 4wt.% of H_2O can be dissolved (Supplementary Fig. 16). We also assume that magma and excess fluids are fully coupled, which implies that the ascent liberates 1.7 wt.% of H_2O resulting in magma expansion. Considering a density for the magma at 8 km depth of 2500 kg/m^3, the mass of magma that would be transferred from 8 to 4 km to account for the deflation estimated at 8 km during T7 (Table 1) is:

$$m_{magma} = 1.32 \cdot 10^6\,[m^3] \cdot 2500\,\left[kg\,m^{-3}\right] = 3.3\ \cdot 10^9\,[kg]$$

The total mass of H_2O that would degas from this mass of magma upon ascent to 4 km is:

$$mH_2O = \frac{m_{magma}\,[kg]}{100} \cdot (5.7\,[wt.\%] - [4wt.\%]) = 56.1 \cdot 10^6\,[kg]$$

resulting in a maximum volume increase at 4 km of:

$$\Delta V_{4km} = \frac{mH_2O\,[g]}{18\,[g\,mol^{-1}]} \cdot 90.72 \cdot 10^{-6}\,[m^3\,mol^{-1}] = 0.28 \cdot 10^6\,[m^3]$$

which is more than 30 time smaller than the inflation measured in the same period at 4 km depth. Together with the calculations performed for Scenario A, this implies that also the presence of excess fluids would not be sufficient to explain the inflation estimated at 4 km depth by geodesy.

Scenario C: we consider that the inflation is caused by the exsolution of volatiles following cooling and crystallization of magma at 4 km depth ("second boiling"[59]; Fig. 7C). Considering that the total inflation estimated at 4 km depth (61.6×10^6 m^3; Table 1) is due to the exsolution of H_2O at 4 km depth (molar volume at 4 km depth is 90.72×10^{-6} m^3/mol), this will require a mass of exsolved H_2O equal to:

$$mH_2O = \frac{61.6\ \cdot\ 10^6\,[\mathrm{m}^3]}{90.72\ \cdot 10^{-6}[m^3\,mol^{-1}]} \cdot 0.018\,\left[kg\,mol^{-1}\right] = 12.2 \cdot 10^9\,[kg]$$

Assuming that 4 wt.% of H_2O can be dissolved at 4 km magma, we can calculate the mass of magma that would need to cool to its solidus to exsolve 12.2×10^9 kg of H_2O. This is a minimum estimate, as if the total exsolved H_2O represent only half of the dissolved H_2O, the mass of magma at 4 km depth would have to double:

$$m_{magma} = \frac{mH_2O\,[kg]}{4\,[wt.\%]} \cdot 100[wt.\%] = 305 \cdot 10^9\,[kg]$$

For a density of 2500 kg/m^3 the magma volume amounts to about 0.12 km^3 that would have cooled to its solidus temperature since the beginning of the inflation in 2007 (Fig. 1). Because at the time of writing the inflation continues, the estimates volume of magma that would have cooled to the solidus increases accordingly.

We also computed the timescale of cooling for a sheet of magma of 100 m thickness and 650 m radius (sufficient magma volume to obtain the required excess fluid to explain inflation), emplaced at 4 km depth at a temperature of 1200 °C (T_m) in a host rock at a temperature of 600 °C (T_w), using a 1D thermal model[74]:

$$T = T_w + \frac{T_m + T_w}{2}\left[\mathrm{erf}\left(\frac{z-b}{2\sqrt{kt}}\right) - \mathrm{erf}\left(\frac{z+b}{2\sqrt{kt}}\right)\right]$$

where z is the vertical coordinate, b is the half thickness of the sheet, k is the thermal conductivity (6.21×10^{-7} m^2/s[75]).

Scenario D: in this scenario, magma rising from 8 km depth (at 900 °C) is supposed to release fluids that separate from the ascending magma and generate the inflation at 4 km depth (Fig. 7 and Supplementary Fig. 15). In this case we calculate the total amount of magma that should degas to release a volume of fluid that at 4 km corresponds to the volume increase estimated by geodesy. The moles of H_2O required at 4 km depth to explain inflation are given by (using T7 as an example; Table 1):

$$mH_2O = \frac{61.6\ \cdot\ 10^6\,[\mathrm{m}^3]}{90.72\ \cdot 10^{-6}[m^3\,mol^{-1}]} \cdot 0.018\,\left[kg\,mol^{-1}\right] = 12.2 \cdot 10^9\,[kg]$$

The minimum mass of magma ascending from 8 km and releasing sufficient excess fluids to explain inflation at 4 km is calculated considering that this decompression will lead to the release of 1.7 wt.% of H_2O (Supplementary Fig. 16):

$$m_{magma} = \frac{12.2 \cdot 10^9\,[kg] \cdot 100[wt.\%]}{1.7\,[wt.\%]} = 7.2 \cdot 10^{11}\,[kg]$$

Considering a magma density of 2500 kg/m^3, at 8 km depth, such mass corresponds to a volume of 0.28 km^3.

Scenario E: this scenario simply considers that the volumetric inflation recorded at 4 km is entirely related to the injection of an equal amount of magma and excess volatiles at 4 km depth.

Data availability

InSAR data of the Campi Flegrei caldera[17] updated to 2023 are freely available at http://www.geosar-iridium.ct.ingv.it/landing/ts_page.php. GNSS time series data are also freely available[15,46,62]. Seismic data are from https://terremoti.ov.ingv.it/gossip/flegrei/.

Code availability

MSC-Marc® software was used for this work and is commercially available. The Fortran code for the inversions (sampling and appraisal stages) is freely available[47,48].

Received: 8 February 2024; Accepted: 28 August 2024;
Published online: 13 September 2024

References

1. Beauducel, F., Peltier, A., Villié, A. & Suryanto, W. Mechanical imaging of a volcano plumbing system from GNSS unsupervised modeling. *Geophys. Res. Lett.* **47**, e2020GL089419 (2020).
2. Acocella, V. et al. Towards scientific forecasting of magmatic eruptions. *Nat. Rev. Earth Environ.* **5**, 5–22 (2023).
3. Dzurisin, D. *Volcano Deformation*. *Volcano Deformation* (Springer Berlin Heidelberg, 2007). https://doi.org/10.1007/978-3-540-49302-0.

4. Amoruso, A. et al. Clues to the cause of the 2011–2013 Campi Flegrei caldera unrest, Italy, from continuous GPS data. *Geophys. Res. Lett.* **41**, 3081–3088 (2014).
5. D'Auria, L. et al. Magma injection beneath the urban area of Naples: A new mechanism for the 2012-2013 volcanic unrest at Campi Flegrei caldera. *Sci. Rep.* **5**, 1–11 (2015).
6. Trasatti, E., Polcari, M., Bonafede, M. & Stramondo, S. Geodetic constraints to the source mechanism of the 2011-2013 unrest at Campi Flegrei (Italy) caldera. *Geophys. Res. Lett.* **42**, 3847–3854 (2015).
7. Gottsmann, J., Camacho, A. G., Tiampo, K. F. & Fernández, J. Spatiotemporal variations in vertical gravity gradients at the Campi Flegrei caldera (Italy): A case for source multiplicity during unrest? *Geophys. J. Int*. (2006) https://doi.org/10.1111/j.1365-246X.2006.03157.x.
8. Battaglia, M., Troise, C., Obrizzo, F., Pingue, F. & De Natale, G. Evidence for fluid migration as the source of deformation at Campi Flegrei caldera (Italy). *Geophys. Res. Lett*. **33**, L01307 (2006).
9. Nespoli, M., Belardinelli, M. E. & Bonafede, M. Stress and deformation induced in layered media by cylindrical thermo-poro-elastic sources: An application to Campi Flegrei (Italy). *J. Volcanol. Geotherm. Res.* **415**, 107269 (2021).
10. Chiodini, G. et al. Magmas near the critical degassing pressure drive volcanic unrest towards a critical state. *Nat. Commun.* **7**, 1–9 (2012).
11. Buono, G. et al. New insights into the recent magma dynamics under Campi Flegrei caldera (Italy) from petrological and geochemical evidence. *J. Geophys. Res. Solid Earth* **127**, e2021JB023773 (2022).
12. Piochi, M. et al. The volcanic and geothermally active Campi Flegrei caldera: An integrated multidisciplinary image of its buried structure. *International Journal of Earth Sciences* **103**, 401–421 (2014).
13. Todesco, M., Rinaldi, A. P. & Bonafede, M. Modeling of unrest signals in heterogeneous hydrothermal systems. *J. Geophys. Res. Solid Earth* **115**, B09213 (2010).
14. Del Gaudio, C., Aquino, I., Ricciardi, G. P., Ricco, C. & Scandone, R. Unrest episodes at Campi Flegrei: A reconstruction of vertical ground movements during 1905-2009. *J. Volcanol. Geotherm. Res.* **195**, 48–56 (2010).
15. De Martino, P., Dolce, M., Brandi, G., Scarpato, G. & Tammaro, U. The ground deformation history of the neapolitan volcanic area (Campi flegrei caldera, somma–vesuvius volcano, and ischia island) from 20 years of continuous gps observations (2000–2019). *Remote Sens* **13**, 2725 (2021).
16. Bevilacqua, A. et al. Data analysis of the unsteadily accelerating GPS and seismic records at Campi Flegrei caldera from 2000 to 2020. *Sci. Rep.* **12**, 19175 (2022).
17. Polcari, M. et al. Thirty years of volcano geodesy from space at Campi Flegrei caldera (Italy). *Sci. Data 2022 91* **9**, 1–13 (2022).
18. Osservatorio Vesuviano INGV. *Bollettino di Sorveglianza Campi Flegrei Dicembre 2023*. https://www.ov.ingv.it/index.php/monitoraggio-e-infrastrutture/bollettini-tutti/bollett-mensili-cf/anno-2023-1/1506-bollettino-mensile-campi-flegrei-2023-12/file (2023).
19. Orsi, G., Di Vito, M. A. & Isaia, R. Volcanic hazard assessment at the restless Campi Flegrei caldera. *Bull. Volcanol.* **66**, 514–530 (2004).
20. Danesi, S., Pino, N. A., Carlino, S. & Kilburn, C. R. J. Evolution in unrest processes at Campi Flegrei caldera as inferred from local seismicity. *Earth Planet. Sci. Lett.* **626**, 118530 (2024).
21. Tramelli, A., Giudicepietro, F., Ricciolino, P. & Chiodini, G. The seismicity of Campi Flegrei in the contest of an evolving long term unrest. *Sci. Rep.* **12**, 2900 (2022).
22. Tramelli, A. et al. Statistics of seismicity to investigate the Campi Flegrei caldera unrest. *Sci. Rep.* **11**, 1–10 (2021).
23. Dipartimento Protezione Civile. *Commissione grandi rischi - comunicato stampa*. https://www.protezionecivile.gov.it/it/comunicato-stampa/protezione-civile-commissione-grandi-rischi-intensificare-attivita-su-campi-flegrei/ (2023).
24. Chiodini, G. et al. The Hydrothermal System of the Campi Flegrei Caldera, Italy. in *Active Volcanoes of the World* 239–255 (Springer Science and Business Media Deutschland GmbH, 2022). https://doi.org/10.1007/978-3-642-37060-1_9.
25. Tamburello, G. et al. Escalating CO2 degassing at the Pisciarelli fumarolic system, and implications for the ongoing Campi Flegrei unrest. *J. Volcanol. Geotherm. Res.* **384**, 151–157 (2019).
26. Caliro, S., Chiodini, G. & Paonita, A. Geochemical evidences of magma dynamics at Campi Flegrei (Italy). *Geochim. Cosmochim. Acta* **132**, 1–15 (2014).
27. Belardinelli, M. E., Bonafede, M. & Nespoli, M. Stress heterogeneities and failure mechanisms induced by temperature and pore-pressure increase in volcanic regions. *Earth Planet. Sci. Lett.* **525**, 115765 (2019).
28. Chiodini, G. et al. Hydrothermal pressure-temperature control on CO2 emissions and seismicity at Campi Flegrei (Italy). *J. Volcanol. Geotherm. Res.* **414**, 107245 (2021).
29. Chiodini, G. et al. Evidence of thermal-driven processes triggering the 2005-2014 unrest at campi flegrei caldera. *Earth Planet. Sci. Lett.* **414**, 58–67 (2015).
30. Calò, M. & Tramelli, A. Anatomy of the Campi Flegrei caldera using Enhanced Seismic Tomography Models. *Sci. Rep.* **8**, 1–12 (2018).
31. Zollo, A. et al. Seismic reflections reveal a massive melt layer feeding Campi Flegrei caldera. *Geophys. Res. Lett*. **35**, L12306 (2008).
32. Kilburn, C. R. J., De Natale, G. & Carlino, S. Progressive approach to eruption at Campi Flegrei caldera in southern Italy. *Nat. Commun.* **8**, 1–8 (2017).
33. Kilburn, C. R. J., Carlino, S., Danesi, S. & Pino, N. A. Potential for rupture before eruption at Campi Flegrei caldera, Southern Italy. *Commun. Earth Environ.* **4**, 1–12 (2023).
34. Amoruso, A., Crescentini, L. & Sabbetta, I. Paired deformation sources of the Campi Flegrei caldera (Italy) required by recent (1980-2010) deformation history. *J. Geophys. Res. Solid Earth* **119**, 858–879 (2014).
35. Pepe, S. et al. Volcanic structures investigation through SAR and seismic interferometric methods: The 2011–2013 Campi Flegrei unrest episode. *Remote Sens. Environ.* **234**, 111440 (2019).
36. Castaldo, R., Tizzani, P. & Solaro, G. Inflating source imaging and stress/strain field analysis at Campi Flegrei caldera: The 2009–2013 unrest episode. *Remote Sensing* **13**, 2298 (2021).
37. Bonafede, M. et al. Source Modelling from Ground Deformation and Gravity Changes at the Campi Flegrei Caldera, Italy. in *Active Volcanoes of the World* 283–309 (Springer Science and Business Media Deutschland GmbH, 2022). https://doi.org/10.1007/978-3-642-37060-1_11.
38. Amoruso, A. & Crescentini, L. Clues of Ongoing Deep Magma Inflation at Campi Flegrei Caldera (Italy) from Empirical Orthogonal Function Analysis of SAR Data. *Remote Sens* **14**, 5698 (2022).
39. Chiarabba, C. & Moretti, M. An insight into the unrest phenomena at the Campi Flegrei caldera from Vp and Vp/Vs tomography. *Terra Nov* **18**, 373–379 (2006).
40. Trasatti, E., Bonafede, M., Ferrari, C., Giunchi, C. & Berrino, G. On deformation sources in volcanic areas: Modeling the Campi Flegrei (Italy) 1982-84 unrest. *Earth Planet. Sci. Lett.* **306**, 175–185 (2011).
41. Trasatti, E., Magri, C., Acocella, V., Del Gaudio, C., Ricco, C., & Di Vito, M.A. Magma transfer at Campi Flegrei caldera (Italy) after the 1538 AD eruption. *Geophys. Res. Lett.* **50**, e2022GL102437 (2023).
42. Amoruso, A., Crescentini, L., D'Antonio, M. & Acocella, V. Thermally-assisted Magma Emplacement Explains Restless Calderas. *Sci. Rep.* **7**, 1–9 (2017).

43. Pappalardo, L. & Mastrolorenzo, G. Rapid differentiation in a sill-like magma reservoir: A case study from the campi flegrei caldera. *Sci. Rep.* **2**, 1–10 (2012).
44. Costanzo, M. R. & Nunziata, C. Inferences on the lithospheric structure of Campi Flegrei District (southern Italy) from seismic noise cross-correlation. *Phys. Earth Planet. Inter.* **265**, 92–105 (2017).
45. Giacomuzzi, G., Chiarabba, C., Bianco, F., De Gori, P. & Agostinetti, N. P. Tracking transient changes in the plumbing system at Campi Flegrei Caldera. *Earth Planet. Sci. Lett.* **637**, 118744 (2024).
46. De Martino, P. et al. Four Years of Continuous Seafloor Displacement Measurements in the Campi Flegrei Caldera. *Front. Earth Sci.* **8**, 615178 (2020).
47. Sambridge, M. Geophysical inversion with a neighbourhood algorithm - II. Appraising the ensemble. *Geophys. J. Int.* **138**, 727–746 (1999).
48. Sambridge, M. Geophysical inversion with a neighbourhood algorithm - I. Searching a parameter space. *Geophys. J. Int.* **138**, 479–494 (1999).
49. Trasatti, E., Giunchi, C. & Agostinetti, N. P. Numerical inversion of deformation caused by pressure sources: Application to Mount Etna (Italy). *Geophys. J. Int.* **172**, 873–884 (2008).
50. Trasatti, E. et al. Bayesian source inference of the 1993-1997 deformation at Mount Etna (Italy) by numerical solutions. *Geophys. J. Int.* **177**, 806–814 (2009).
51. Davis, P. M. Surface deformation due to inflation of an arbitrarily oriented triaxial ellipsoidal cavity in an elastic half-space, with reference to Kilauea volcano, Hawaii. *J. Geophys. Res. Solid Earth* (1986) https://doi.org/10.1029/jb091ib07p07429.
52. Gregg, P. M., De Silva, S. L., Grosfils, E. B. & Parmigiani, J. P. Catastrophic caldera-forming eruptions: Thermomechanics and implications for eruption triggering and maximum caldera dimensions on Earth. *J. Volcanol. Geotherm. Res*. **241–242**, 1–12 (2012).
53. Currenti, G., Bonaccorso, A., Del Negro, C., Scandura, D. & Boschi, E. Elasto-plastic modeling of volcano ground deformation. *Earth Planet. Sci. Lett.* **296**, 311–318 (2010).
54. Trasatti, E. Volcanic and Seismic source Modelling (VSM). *The Python toolkit for modelling geodetic data*. (2022) https://doi.org/10.24424/T83F-5T97.
55. Di Vito, M. A. et al. Magma transfer at Campi Flegrei caldera (Italy) before the 1538 AD eruption. *Sci. Rep.* **6**, 32245 (2016).
56. Head, M., Hickey, J., Gottsmann, J. & Fournier, N. The Influence of Viscoelastic Crustal Rheologies on Volcanic Ground Deformation: Insights From Models of Pressure and Volume Change. *J. Geophys. Res. Solid Earth* **124**, 8127–8146 (2019).
57. Simo, J. C. & Ju, J. W. Strain- and stress-based continuum damage models-I. Formulation. *Int. J. Solids Struct.* **23**, 821–840 (1987).
58. Rivalta, E. & Segall, P. Magma compressibility and the missing source for some dike intrusions. *Geophys. Res. Lett*. **35**, 04306 (2008).
59. Tait, S., Jaupart, C. & Vergniolle, S. Pressure, gas content and eruption periodicity of a shallow, crystallising magma chamber. *Earth Planet. Sci. Lett.* **92**, 107–123 (1989).
60. Townsend, M., Huber, C., Degruyter, W. & Bachmann, O. Magma Chamber Growth During Intercaldera Periods: Insights From Thermo-Mechanical Modeling With Applications to Laguna del Maule, Campi Flegrei, Santorini, and Aso. *Geochemistry. Geophys. Geosystems* **20**, 1574–1591 (2019).
61. Caricchi, L., Biggs, J., Annen, C. & Ebmeier, S. The influence of cooling, crystallisation and re-melting on the interpretation of geodetic signals in volcanic systems. *Earth Planet. Sci. Lett*. **388**, 166-174 (2014).
62. De Martino, P., Dolce, M., Brandi, G. & Scarpato, G. *Campi Flegrei cGPS Weekly Positions Time Series*. (2023) https://doi.org/10.5281/zenodo.10082465.
63. Trombetti, T. et al. On the seafloor horizontal displacement from cGPS and compass data in the Campi Flegrei caldera. *J. Geod.* **97**, 1–15 (2023).
64. Wegmüller, U. & Werner, C. Gamma SAR processor and interferometry software. *Eur. Sp. Agency*, (Special Publ. ESA SP 1687–1692 (1997).
65. Cayol, V. & Cornet, F. H. Effects of topography on the interpretation of the deformation field of prominent volcanoes - Application to Etna. *Geophys. Res. Lett.* https://doi.org/10.1029/98gl51512 (1998).
66. Agip. *Geologia e geofisica del sistema geotermico dei Campi Flegrei*. Technical report (Settore Esplorazione) (1987).
67. Trasatti, E. Volcanic and seismic source modeling: An open tool for geodetic data modeling. *Front. Earth Sci*. **10**, https://doi.org/10.3389/feart.2022.917222 (2022).
68. Mindlin, R. D. Force at a point in the interior of a semi-infinite solid. *J. Appl. Phys.* **7**, 195–202 (1936).
69. Eshelby, J. D. The determination of the elastic field of an ellipsoidal inclusion, and related problems. *Proc. R. Soc. London. Ser. A. Math. Phys. Sci.* **241**, 376–396 (1957).
70. Amoruso, A. & Crescentini, L. Shape and volume change of pressurized ellipsoidal cavities from deformation and seismic data. *J. Geophys. Res. Solid Earth* **114**, B02210 (2009).
71. Ricco, C., Petrosino, S., Aquino, I., Del Gaudio, C. & Falanga, M. Some investigations on a possible relationship between ground deformation and seismic activity at campi flegrei and ischia volcanic areas (Southern Italy). *Geosciences* **9**, 222 (2019).
72. Pitzer, K. S. & Sterner, S. M. Equations of state valid continuously from zero to extreme pressures for H2O and CO2. *J. Chem. Phys.* **101**, 3111–3116 (1994).
73. Judenherc, S. & Zollo, A. The Bay of Naples (southern Italy): Constraints on the volcanic structures inferred from a dense seismic survey. *J. Geophys. Res. Solid Earth* **109**, 10312 (2004).
74. Jaeger, J. C. Application of the Theory Of Heat Conduction to Geothermal Measurements. in (2013). https://doi.org/10.1029/gm008p0007.
75. Whittington, A. G., Hofmeister, A. M. & Nabelek, P. I. Temperature-dependent thermal diffusivity of the Earth's crust and implications for magmatism. *Nature* **458**, 319–321 (2009).

Acknowledgements

We thank Anna Tramelli for providing seismic tomography and for useful discussions. Guido Ventura provided friendly discussions and valuable hints. Lucia Pappalardo is also acknowledged for useful discussions. Francesco Maccaferri and Andrea Antonioli contributed with useful hints. The authors wish to thank all the many colleagues contributing to the Campi Flegrei monitoring systems. The authors are particularly indebted to the INGV's technical staff ensuring the 24/7 functioning of the seismic and GNSS monitoring networks. We thank Nico Fournier, James Hickey and an anonymous reviewer for their careful review. A.A. is funded by the LOVE-CF project (2020-2024) "Linking Surface Observables to sub-Volcanic Plumbing-System: A Multidisciplinary Approach for Eruption Forecasting at Campi Flegrei Caldera (Italy)", funded by INGV (Internal Register no. 1865 17/07/2020).

Author contributions

A.A. modelling. E.T. concept and modelling. L.C. modelling and interpretation. M.P. and PDM data analysis. V.A. concept and interpretation. M.D.V. concept and interpretation. All authors equally contributed to the writing.

Competing interests

The authors declare no competing interests.

Additional information

Supplementary information The online version contains supplementary material available at https://doi.org/10.1038/s43247-024-01665-4.

Correspondence and requests for materials should be addressed to Elisa Trasatti.

Peer review information *Communications Earth & Environment* thanks James Hickey, Nico Fournier and the other, anonymous, reviewer(s) for their contribution to the peer review of this work. Primary Handling Editors: Emma Liu and Carolina Ortiz Guerrero. A peer review file is available.